ACCEPTED ARTICLE PREVIEW

Accepted Article Preview: Published ahead of online publication

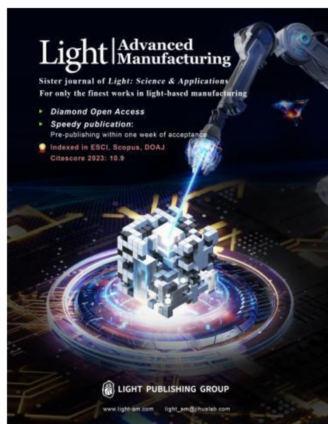

Physically Covariant, Curvilinear Thick-mask Model for Full-chip Computational Lithography

Haofeng Chen, Shaopeng Guo, Kaixuan Su, Song Zhang, Hao Jiang, David H. Wei and Shiyuan Liu

Cite this article as: Haofeng Chen, Shaopeng Guo, Kaixuan Su, Song Zhang, Hao Jiang, David H. Wei and Shiyuan Liu. Physically Covariant, Curvilinear Thick-mask Model for Full-chip Computational Lithography. *Light: Advanced Manufacturing* accepted article preview 11 June 2026; doi: 10.37188/lam.2026.100

This is a PDF file of an unedited peer-reviewed manuscript that has been accepted for publication. LAM are providing this early version of the manuscript as a service to our customers. The manuscript will undergo copyediting, typesetting and a proof review before it is published in its final form. Please note that during the production process errors may be discovered which could affect the content, and all legal disclaimers apply.

Received 4 December 2025; revised 9 June 2026; accepted 10 June 2026;
Accepted article preview online 11 June 2026

Accepted Manuscript

ACCEPTED ARTICLE PREVIEW

1
2 # Physically Covariant, Curvilinear Thick-mask Model for Full-chip Computational Lithography

3 **Haofeng Chen[1], Shaopeng Guo[1], Kaixuan Su[1], Song Zhang[1,2], Hao Jiang[1, *],**
4 **David H. Wei[2,3, *], and Shiyuan Liu[1,2, *]**

5 [1] School of Mechanical Science and Engineering, Huazhong University of Science
6 and Technology, Wuhan 430074, China.

7 [2] Yuwei Optica Co., Ltd., Wuhan, 430070, Hubei, China.

8 [3] Quantica Computing LLC, San Jose, California 95131, USA

9 *hjiang@hust.edu.cn

10 *david.hq.wei@gmail.com

11 *shyliu@hust.edu.cn

12

13

14

15

16

17

18

Accepted Manuscript

ACCEPTED ARTICLE PREVIEW

Abstract

As semiconductor process nodes advance, the interaction between electromagnetic waves and mask three-dimensional topography becomes increasingly significant. Curvilinear masks with superior process windows are being rapidly adopted, exposing the limitations of existing thick-mask models in accommodating arbitrary curvilinear edges. Therefore, a theoretical framework for the full-chip-scale, rapid modelling of curvilinear thick masks is required. This paper introduces a physically covariant curvilinear thick-mask model based on edge diffraction correction for rapid full-chip layout simulation. The model decomposes the mask response into a thin-mask approximation term and an edge diffraction correction term. Through rigorous mathematical derivation, the diffraction response of the reference mask edges is decomposed into physically meaningful two-dimensional differential edge diffraction kernels. Furthermore, the edge diffraction term of full-chip layouts is efficiently reconstructed via a multi-channel tensor convolution framework, thereby correcting the thin-mask approximation and establishing the curvilinear thick-mask model. Simulation results demonstrated that, compared with finite-difference time-domain benchmarks, the proposed model achieved curvilinear mask near-field root mean square errors below 0.03 while delivering a speed-up of over 2600 times. Moreover, it provided more than 2× error reduction over traditional Manhattanisation curvilinear models and maintained superior physical covariance. This study is expected to provide robust support not only for efficient and accurate forward modelling in resolution-enhancement techniques, such as inverse lithography technology and source mask optimisation, but also for the optical characteristic fast simulation of metasurfaces and metamaterials.

Keywords: curvilinear thick-mask model, edge diffraction correction, differential edge diffraction kernels (DEDKs), tensor convolution, physical covariance, full-chip, computational lithography

Accepted Manuscript

ACCEPTED ARTICLE PREVIEW

Introduction

Lithography, the core process in semiconductor manufacturing, transfers mask patterns onto a wafer resist with high precision using an objective lens system [1, 2]. Computational lithography (CL) combines the electromagnetic simulation of the lithography process with optimisation algorithms to accurately achieve wafer patterns with high fidelity to the designed layout. This capability compensates for exposure deviations while enhancing pattern density and yield, establishing CL as a critical enabler for shrinking advanced technology nodes [3-5]. Functioning as a core component of CL models, the mask model is responsible for rapidly and accurately characterising the physical interaction between electromagnetic waves and the mask structure, with the mask near-field distribution serving as its output [6]. Physical covariance is a key indicator for evaluating the mask model performance, and it requires the outputs of the model for identical mask layouts to be invariant under translation and rotation [7]. This characteristic not only reflects the inherent physics of mask electromagnetic effects, but also ensures consistent optimisation results for identical design patterns during resolution-enhancement flows, such as optical proximity correction [8]. For 193 nm deep ultraviolet (DUV) lithography, as the critical dimensions (CD) shrink to the 45 nm node and below, electromagnetic interactions with mask three-dimensional topography become increasingly complex and pronounced. This renders traditional Kirchhoff-based thin-mask approximations inadequate [9, 10]. Concurrently, the development of inverse lithography technology (ILT) has broken free from the constraints of traditional 'Manhattan' mask layouts [11-13]. The adoption of all-angle edges significantly expands the process window while improving CD uniformity and sidelobe printing control [14-16]. Furthermore, the maturation of multibeam mask writing [17] and the standardisation of curvilinear mask data formats [18] have accelerated the industrial adoption of curvilinear masks [19]. In this context, developing thick-mask models that can efficiently and accurately characterise 3D electromagnetic effects on

Accepted Manuscript

ACCEPTED ARTICLE PREVIEW

1 curvilinear mask layouts while maintaining physical covariance has become a
2 pressing challenge in CL [20].

3 Although rigorous numerical solutions to Maxwell's equations, such as
4 finite-difference time-domain (FDTD) [21], rigorous coupled-wave analysis [22], and
5 waveguide [23], can accurately resolve mask near-fields, they are computationally
6 prohibitive for full-chip mask layouts owing to memory and runtime constraints.
7 Various thick-mask approximation techniques have been developed to balance the
8 accuracy and efficiency [9, 10]. To exploit the translational and rotational invariance of
9 electromagnetic effects, a common strategy involves extracting electromagnetic
10 responses for a set of representative structures via rigorous simulation and then
11 compositing these responses into near-rigorous full-chip models using the domain
12 decomposition method (DDM) [24]. Alternatively, these rigorously simulated responses
13 can be used to derive boundary corrections for the thin-mask model under the
14 Kirchhoff approximation, such as the boundary layer model [25] and edge-filter model [9,
15 26]. Note that signal processing principles from other optical domains can inform the
16 extraction of key electromagnetic responses in thick-mask modelling [27]. With the
17 development of computer technology, deep-learning and machine-learning methods
18 have been applied to develop efficient thick-mask models [28-30]. These thick-mask
19 models predominantly address Manhattan geometries with a constrained orientation
20 diversity. The growing adoption of curvilinear masks has considerably increased
21 pattern complexity and introduced intricate diffraction effects that challenge
22 traditional models in terms of efficiency, accuracy, and the preservation of physical
23 covariance [31]. Early approaches to modelling curvilinear edges relied on
24 Manhattanisation, in which curves were approximated by orthogonal segments,
25 thereby incurring inherent geometric errors and degrading the physical covariance [32].
26 Subsequent Mask3D kernel models extract direction-dependent filter functions from
27 rigorous simulations [20, 33, 34]; however, they still face fundamental challenges in
28 achieving a real-time, physically covariant alignment of these kernels with arbitrarily

Accepted Manuscript

ACCEPTED ARTICLE PREVIEW

1 oriented edges at full-chip scale. Table 1 compares representative thick-mask models
2 to distinguish the present study from prior thick-mask modelling approaches.

3 **Table 1** Comparison of representative thick-mask models

Model	Rigorous simulation based	Mask pattern type	Topology-decoupled kernel	Explicit full-chip modelling framework	Physically -covariant preserved
DDM / edge-filter model	✓	Manhattan	✕	✓	✕
Manhattanisation-based model	✓	Curvilinear (approximated)	✕	✓	✕
Earlier Mask3D kernel model	✓	Curvilinear	✓	✕	✕
Proposed model	✓	Curvilinear	✓	✓	✓

4 As shown in Table 1, DDM- and Manhattanisation-based models can support
5 full-chip modelling by pre-characterising a finite set of edge orientations; however,
6 their applicability is still fundamentally limited to Manhattan or
7 discretised-orientation structures. The earlier all-angle Mask3D kernel model
8 introduced a local response kernel decoupled from the layout topology; however, it
9 did not explicitly establish a physically covariant full-chip modelling framework for
10 arbitrarily oriented curvilinear edges. In summary, these common limitations indicate
11 three key challenges: (1) extracting differential edge diffraction functions that are
12 decoupled from specific mask geometries and thus adaptable to arbitrary curvilinear
13 layouts; (2) establishing a physically covariant relationship between these differential
14 edge diffraction functions and the curvilinear edges of arbitrary orientation to ensure
15 model accuracy; and (3) achieving the rapid, full-chip reconstruction of the diffracted
16 field while preserving the covariant relation to meet the computational efficiency
17 requirements. Therefore, it is necessary to develop a novel framework to address these
18 challenges effectively.

Accepted Manuscript

ACCEPTED ARTICLE PREVIEW

This paper introduces a physically covariant curvilinear thick-mask model based on edge diffraction correction for rapid full-chip layout simulation. Initially, a vectorial mask transmission matrix was introduced to characterise the electromagnetic wave propagation through the mask, and matrix transformations were used to establish the covariant relationship between the polarisation components and the curvilinear mask edges. By expanding the transmission matrix into a power series and truncating it, we formulated the mask model as a linear superposition of a thin-mask approximation term and an edge diffraction correction term. This expression establishes a diffraction-correction-based theoretical framework for a thick-mask model applicable to full-chip curvilinear layouts. Within this theoretical framework, by combining the projection-slice theorem [35, 36] with electromagnetic diffraction principles, we mathematically decompose the 1D edge diffraction responses obtained from rigorous simulations into 2D differential edge diffraction kernels (DEDKs). These kernels represent the intrinsic diffraction response of an elementary edge and are decoupled from the specific mask topologies. Furthermore, to address the angular dependence of these DEDKs, we exploited their rotational symmetry in the spatial domain to establish a real-time physical covariant mapping between the DEDKs and the curvilinear edges of arbitrary orientations. Accordingly, a nine-channel tensor convolution was used to perform the path integration of DEDKs along the curvilinear edges, enabling the rapid reconstruction of the full-chip mask diffraction term. This reconstructed term was subsequently applied to correct the Kirchhoff thin-mask approximation, yielding a physically covariant thick-mask model that enables the efficient and accurate simulation of curvilinear layouts. The combination of speed and accuracy renders this model highly valuable for resolution-enhancement techniques applied in the lithography of curvilinear masks.

Principle

Thick-mask model framework

Accepted Manuscript

ACCEPTED ARTICLE PREVIEW

1 In the CL framework, the primary role of the mask model is to characterise the
2 transformation of the incident electromagnetic field vector $\left[E_X^{in}(x,y),E_Y^{in}(x,y)\right]^{\mathrm{T}}$
3 into the near-field output $[E_X^{out}(x,y),E_Y^{out}(x,y)]^{\mathrm{T}}$ after interaction with the mask
4 structure. This physical process can be abstractly represented as

5
$$\begin{bmatrix} E_X^{out}(x,y) \\ E_Y^{out}(x,y) \end{bmatrix} = \begin{bmatrix} M_X^X(x,y) & M_X^Y(x,y) \\ M_Y^X(x,y) & M_Y^Y(x,y) \end{bmatrix} \begin{bmatrix} E_X^{in}(x,y) \\ E_Y^{in}(x,y) \end{bmatrix} \tag{1}$$

6 where (x, y) are the spatial coordinates on the mask plane, and the matrices
7 $\left[M_X^X(x,y),M_X^Y(x,y);M_Y^X(x,y),M_Y^Y(x,y)\right]$ constitute the spatially varying Jones matrix
8 of the mask, serving as the polarisation-dependent mathematical model of the mask,
9 denoted simply as **M**.

10 During the 3D mask–electromagnetic wave interaction, thick-mask effects
11 originate primarily from complex electromagnetic boundary perturbations at the mask
12 edges, in contrast to the simplified boundary assumptions of thin-mask models. By
13 leveraging this physical mechanism, we propose a curvilinear thick-mask model that
14 incorporates edge-diffraction corrections, thereby extending the conventional
15 Kirchhoff thin-mask approximation. Specifically, the electromagnetic response of the
16 mask to the layout pattern can be approximately decomposed as

17
$$\mathbf{M}(x,y) = \mathbf{M_0}[A(x,y)] + \mathbf{M_1}[\partial A(x,y)] + o(\mathbf{M_n}[A(x,y)]) \tag{2}$$

18 where $\mathbf{M}_0[A(x, y)]$ is the thin-mask term representing the ideal geometric transmission
19 and is an affine function of the mask area indicator function $A(x, y)$. $\mathbf{M}_1[\partial A(x, y)]$
20 constitutes the first-order edge diffraction correction, whose accurate and efficient
21 modelling presents the central challenge in the thick-mask model. This term depends
22 on the vector field of mask edges $\partial A(x, y)$, and can be obtained by integrating the
23 rigorously simulated DEDK along the mask edges. The term $o(\mathbf{M}_n[A(x, y)])$ captures
24 the higher-order diffraction effects that depend on the mask pattern and involve
25 complex spatial interactions. In principle, such higher-order contributions can be

Accepted Manuscript

ACCEPTED ARTICLE PREVIEW

1 obtained through rigorous simulations. Given the high-frequency cut-off imposed by
2 the numerical aperture (NA) of the projection lens and the inherently small amplitude
3 of this term, and in accordance with mainstream approximate thick-mask modelling
4 practices [20, 33], higher-order diffraction effects are omitted to balance computational
5 efficiency with accuracy. As the CD continues to shrink, higher-order diffraction
6 contributions, such as coupling effects between adjacent mask edges, may become
7 more pronounced. Nevertheless, owing to the inherently scalable architecture of the
8 model, such higher-order effects can be incorporated in a manner analogous to the
9 first-order edge correction. The corresponding higher-order diffraction kernels were
10 extracted from rigorous simulations of masks with various CDs via 1D
11 projection-slice and circular harmonic decomposition techniques, and a similar
12 path-integral procedure was then applied to quantify their influence, thereby
13 progressively improving the predictive accuracy.

14 Within the thick-mask modelling framework established in Eq. (2), the thin-mask
15 component $\mathbf{M_0}[A(x, y)]$ is directly mapped from the mask layout and is defined as

16
$$\mathbf{M_0}[A(x,y)] = \begin{cases} t_{\text{bright}}\mathbf{I}, A(x,y) \in \text{clear region} \\ t_{\text{dark}}\mathbf{I}, A(x,y) \in \text{otherwise} \end{cases} \quad (3)$$

17 where $\mathbf{I}$ is a 2×2 identity matrix, and t_{bright} and t_{dark} represent the complex transmission
18 coefficients of the bright and dark regions, respectively. These coefficients can be
19 obtained either experimentally or theoretically using the thin-film transfer-matrix
20 method [37]. The edge diffraction correction term $\mathbf{M_1}[\partial A(x, y)]$ in a thick-mask model
21 depends not only on the material properties of the mask but also on the local
22 orientation of each edge segment. The efficient construction of this term with high
23 accuracy for curvilinear masks is critical for ensuring the computational accuracy and
24 efficiency of the proposed model, and will be the focus of our subsequent theoretical
25 development.

26 **Generation of differential edge diffraction kernels**

Accepted Manuscript

ACCEPTED ARTICLE PREVIEW

1 We represent the edge correction term $\mathbf{M_1}[\partial A(x, y)]$ as an integral of the DEDK
2 along the mask edges to attain sufficient geometric freedom for full-chip curvilinear
3 masks. Here, DEDK is a mathematical construction that describes the diffraction
4 response induced by a differential edge segment and cannot be directly measured or
5 simulated in isolation. Instead, subtracting the thin-mask component from a rigorous
6 straight-edge simulation yields a 1D projection of the kernel along the edge direction.
7 According to the projection-slice theorem, the Fourier transform of this projection
8 provides a central slice through a 2D kernel spectrum [35]. Guided by Huygens'
9 principle, we regard the differential edge as a rotationally covariant secondary source
10 so that, in the edge-aligned local coordinate system, the induced radially symmetric
11 response is independent of the absolute orientation of the edge, and a single normal
12 slice is sufficient to recover the full radial spectrum. Because of the vectorial nature of
13 the electromagnetic boundary conditions, we decomposed the frequency-domain
14 slices into even and odd components. The even and odd parts of the DEDK were
15 reconstructed using zero- and first-order circular harmonic transforms, capturing the
16 scalar radial response and antisymmetric normal modulation, respectively. Their
17 superposition reconstructed the complete kernel spectrum, which was then
18 inverse-transformed into a spatial domain. This approach avoids repeated rigorous
19 simulations for varying mask geometries, and provides the necessary flexibility to
20 support the proposed curvilinear thick-mask model.

21 This model employs Maxwell-equation rigorous solvers to analyse the near-field
22 response of the isolated thick-mask edge, thereby obtaining the edge diffraction
23 response for specified geometric configurations. The edge diffraction response
24 depends on the incident conditions and is typically expressed as a polynomial
25 expansion of the incident wave vectors (k_x, k_y) [38, 39]. As this study focused on
26 developing an efficient and physically covariant curvilinear thick-mask model for a
27 full-chip layout, we retained only the zeroth-order term of this expansion under the
28 normal-incidence assumption. The remaining higher-order terms followed a similar

Accepted Manuscript

ACCEPTED ARTICLE PREVIEW

1 construction and are therefore not elaborated here. Under an X-polarised plane wave
2 $E_X^{in} = [1, 0]^T$, the transmitted electric field yields the Jones matrix components
3 $M_X^X(x, y)$ and $M_Y^X(x, y)$. Similarly, the Y-polarised incidences $E_Y^{in} = [0, 1]^T$ provide
4 $M_X^Y(x, y)$ and $M_Y^Y(x, y)$. Fig. 1a depicts the simulations performed for the template of
5 an infinitely long straight-edge mask structure with its surface normal points along the
6 +x-axis. The rigorously computed electromagnetic near-field distribution in Fig. 1b
7 demonstrates that the geometric symmetry constraints reduce the mask response to 1D
8 functions $L_X^X(x)$ and $L_Y^Y(x)$ along the x-axis, which represent co-polarised responses
9 under X- and Y-polarised illumination, respectively, whereas the cross-polarised
10 components $L_Y^X(x)$ and $L_X^Y(x)$ vanish. Consequently, the Jones matrix can be
11 simplified to a diagonal form. According to Eq. (2), the mask response $\mathbf{M}(x)$ is
12 subtracted from the thin-mask term $\mathbf{M}_0(x)$, as shown in Fig. 1c, and the
13 edge-diffraction term $\mathbf{M}_1(x)$ is isolated, as shown in Fig. 1d.

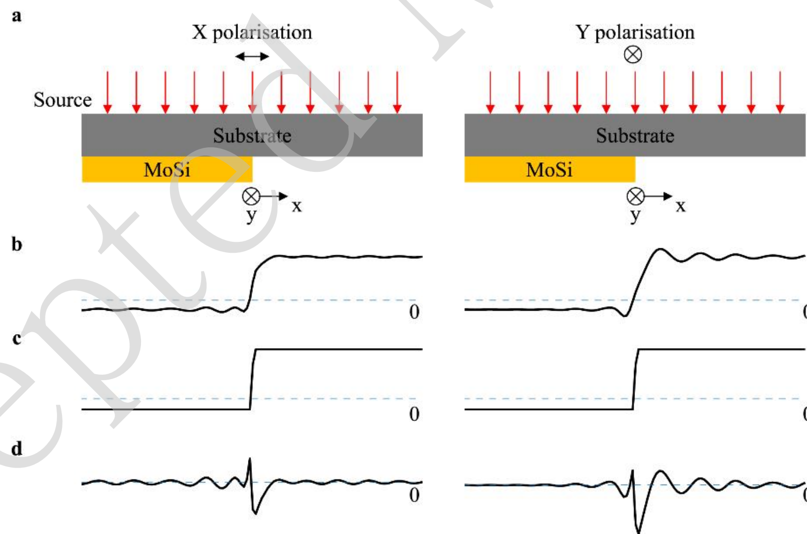

14

15 **Fig. 1** Near-field characteristics of a template phase shift mask (PSM) structure under polarised
16 illumination. **a** Template PSM structure with surface normal along the +x direction, illuminated by
17 normally incident X- and Y-polarised sources. **b** Rigorous mask near-field distributions under X-
18 and Y-polarised illumination. Simulation with sufficiently large periodicity to suppress edge
19 coupling diffraction. **c** Thin-mask term $L_{0,i}^i(x)$, calculated via multi-layer transfer matrix method.

Accepted Manuscript

1 **d** Edge diffraction terms $L^{i}_{1,i}(x)$

2 Here, the 1D edge diffraction term $L^{i}_{1,i}(x)$ represents the projection of the DEDK
3 $M^{i}_{1,i}(x,,y;\mathrm{dy})$ along the y-direction. By applying the projection-slice theorem, which
4 characterises the Radon transform behaviour in the Fourier frequency domain [35, 36], we
5 derived their relationship in the frequency domain:

6 $$\mathbf{FFT}\{M^{i}_{1,i}(x,y;\mathrm{dy})\}(fx,fy=0)=\mathbf{FFT}\{L^{i}_{1,i}(x)\}\stackrel{\mathrm{def}}{=}\tilde{L}^{i}_{1,i}(fx),i=\mathrm{X},\mathrm{Y} \quad (4)$$

7 The Fourier spectrum of the edge diffraction term $\tilde{L}^{i}_{1,i}(fx)$ is mathematically
8 identical to the cross-section of the Fourier transform $\mathbf{FFT}\{M^{i}_{1,i}(x,y;\mathrm{dy})\}$ at *fy*=0.
9 To construct the diffraction kernel generated by the differential edge, the odd–even
10 decomposition method is applied to the spectrum of the edge diffraction term
11 $\tilde{L}^{i}_{1,i}(fx)$, dividing it into two parts: an even component $\tilde{L}^{i,e}_{1,i}(fx)$ representing the
12 static background field (DC transmission term), and an odd component $\tilde{L}^{i,o}_{1,i}(fx)$ that
13 encodes the diffraction modulation along the edge normal. According to Huygens'
14 principle, each differential edge acts as a secondary source, emitting circularly
15 symmetric diffraction perturbations. The Hankel transform reveals that circular
16 symmetry is preserved under the Fourier transform [20]. Fig. 2 shows that the even–odd
17 spectrum induced by the differential edge can be reconstructed by enforcing a circular
18 symmetry operator, and the spatial diffraction field can be obtained using the inverse
19 Fourier transform:

20 $$M^{i,e}_{1,i}(x,y;\mathrm{dy})=\mathbf{IFFT}\left\{\mathbf{circ}\left(\tilde{L}^{i,e}_{1,i}(fx)\right)\right\},i=\mathrm{X},\mathrm{Y} \quad (5)$$

21 $$M^{i,o}_{1,i}(x,y;\mathrm{dy})=\mathbf{IFFT}\left\{\mathbf{circ}\left(\tilde{L}^{i,o}_{1,i}(fx)\right)\cos\varphi\right\},i=\mathrm{X},\mathrm{Y} \quad (6)$$

22 Here, $M^{i,e}_{1,i}(x,y;\mathrm{dy})$ captures the scalar radial response, whereas $M^{i,o}_{1,i}(x,y;\mathrm{dy})$
23 represents the antisymmetric modulation along the edge normal. **circ**() enforces

Accepted Manuscript

ACCEPTED ARTICLE PREVIEW

circular symmetry; the x- and y- axes of the circular symmetry correspond to the normal and tangential directions of the long straight-edge used in the rigorous simulation, respectively. The angle φ is measured in the frequency domain with respect to the edge normal direction (+*fx* axis).

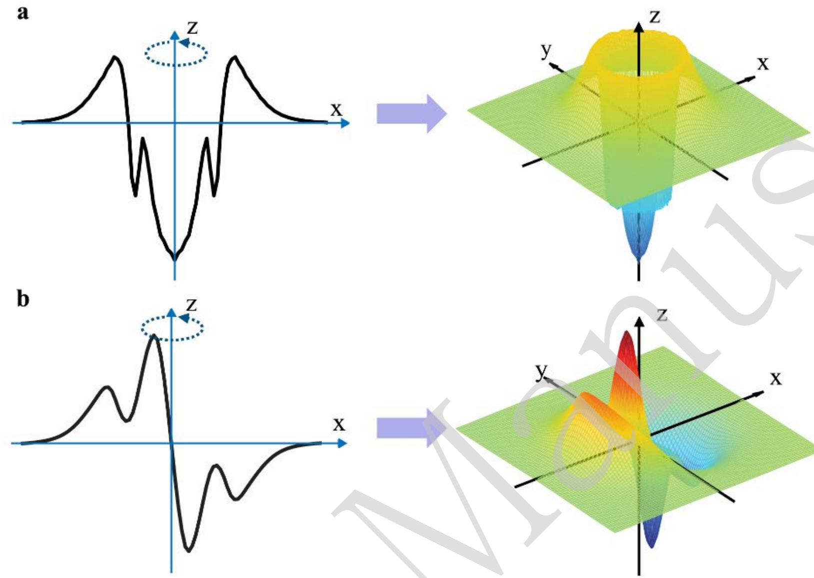

Fig. 2 Spectral reconstruction of even/odd components in the DEDK. **a** The left-side image illustrates the even spectral component $\tilde{L}_{1,i}^{i,e}(fx)$. By performing axisymmetric rotation around the z-axis, the corresponding kernel even component spectrum is shown on the right. **b** The left-side image shows the odd spectral component $\tilde{L}_{1,i}^{i,o}(fx)$. During rotation around the z-axis, an azimuthal modulation factor cosφ is introduced, yielding the odd component spectrum in the right image.

Superimposing even components $M_{1,i}^{i,e}(x, y; \mathrm{dy})$ and odd components $M_{1,i}^{i,o}(x, y; \mathrm{dy})$ generates the DEDK **M₁**(*x*, *y*; dy). This has an evident physical interpretation and is decoupled from the specific mask structure. This property strongly supports the construction of the curvilinear layout diffraction field **M₁**[∂*A*(*x*, *y*)].

Covariant transformation of DEDK

Accepted Manuscript

ACCEPTED ARTICLE PREVIEW

In curvilinear mask layouts, each local edge segment exhibits an arbitrary normal angle in the x–y plane. DEDK, which serves as a physical kernel describing electromagnetic diffraction phenomena, inherently satisfies translational and rotational invariances. Consequently, the differential diffraction response $\mathbf{M}_\mathbf{1}^{\boldsymbol{\theta}}(x, y; \mathrm{dr})$ for an infinitesimal edge segment with local normal angle θ relative to the x-axis satisfies the covariant transformation:

$$\mathbf{M}_\mathbf{1}^{\boldsymbol{\theta}}(x, y; \mathrm{dr}) = \mathbf{R}(-\theta)\mathbf{M}_\mathbf{1}^{\mathbf{rot}}(x, y, \theta; \mathrm{dr})\mathbf{R}(\theta) \tag{7}$$

where $\mathbf{R}(\theta)$ is the 2D rotation matrix, and $\mathbf{M}_\mathbf{1}^{\mathbf{rot}}(x, y, \theta; \mathrm{dr}) = \mathbf{M}_\mathbf{1}(x\cos\theta + y\sin\theta, -x\sin\theta + y\cos\theta; \mathrm{dy})$ represents the rotation of the spatial coordinate system of the diffraction kernel element. Fig. 3 depicts the covariant transform of the DEDK in the local in-plane edge normal direction.

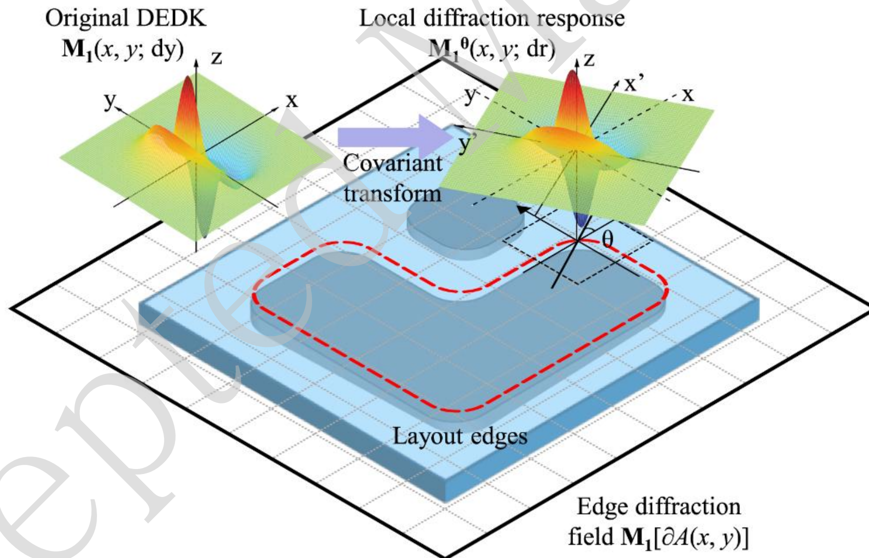

Fig. 3 DEDK transform in the differential edge-normal direction. Starting from the precomputed DEDK component $\mathbf{M_1}(x, y; \mathrm{dy})$ corresponding to a template mask edge structure with its normal along the x-axis, curvilinear pattern edges are discretised into differential elements dr. For each element, the local normal angle θ is computed, and the local diffraction response $\mathbf{M}_\mathbf{1}^{\boldsymbol{\theta}}(x, y; \mathrm{dr})$ is derived through covariant transformation and superimposed at the position of the element in the diffraction field.

Accepted Manuscript

ACCEPTED ARTICLE PREVIEW

1 As discussed in the preceding section, the DEDK decomposes into two
2 components: the even component characterises the static background field, which is
3 insensitive to edge rotation; thus, its impact depends primarily on the edge segment
4 length; and the odd component captures the edge-normal diffractive modulation,
5 requiring rotational transformation to align with the local edge orientation for the
6 accurate modelling of direction-sensitive diffraction effects. This per-element rotation
7 significantly increases both the computational complexity and runtime demands
8 owing to the geometric complexity of the full-chip curvilinear mask. Specifically,
9 $\mathbf{M_1^o}(x, y; \mathrm{dr})$ is the odd component of the circularly symmetric directional kernel. Its
10 rotation can be represented by a trigonometric combination of itself and its orthogonal
11 diffraction modulation components, $[\mathbf{M_1^o}(x, y; \mathrm{dr})]^\mathrm{T}$. This enables real-time
12 alignment between the kernel orientation and the edge geometry, thereby ensuring the
13 physical covariance of the diffraction response. Accordingly, the rotated diffraction
14 response of any differential edge with an angle of θ can be represented as the linear
15 superposition of three field vectors:

16
$$\left(M_{1,i}^{i}\right)^{rot} = M_{1,i}^{i,o} \cos\theta + \left[M_{1,i}^{i,o}\right]^\mathrm{T} \sin\theta + M_{1,i}^{i,e}, i = X, Y \quad (8)$$

17 Combining Eqs. (7) and (8), the local diffraction response $\mathbf{M_1^\theta}(x, y; \mathrm{dr})$ induced
18 by a single edge segment at angle θ is expressed as

19
$$\mathbf{M_1^\theta}(x, y; \mathrm{dr}) = \begin{bmatrix} \cos\theta & \sin\theta \\ -\sin\theta & \cos\theta \end{bmatrix} \begin{bmatrix} M_{1,X}^{X,rot} & 0 \\ 0 & M_{1,Y}^{Y,rot} \end{bmatrix} \begin{bmatrix} cos\,\theta & -sin\,\theta \\ sin\,\theta & cos\,\theta \end{bmatrix}$$

20
$$= \begin{bmatrix} \frac{(M_1^-)^{rot}}{2}\cos 2\theta + \frac{(M_1^+)^{rot}}{2} & -\frac{(M_1^-)^{rot}}{2}\sin 2\theta \\ -\frac{(M_1^-)^{rot}}{2} sin\,2\theta & -\frac{(M_1^-)^{rot}}{2} cos\,2\theta + \frac{(M_1^+)^{rot}}{2} \end{bmatrix} \quad (9)$$

21 where the shorthand notations $M_1^- = M_{1,X}^X(x, y; \mathrm{dy}) - M_{1,Y}^Y(x, y; \mathrm{dy})$ and $M_1^+ =$
22 $M_{1,X}^X(x, y; \mathrm{dy}) + M_{1,Y}^Y(x, y; \mathrm{dy})$ are defined.

Accepted Manuscript

1 **Full-chip curvilinear mask model**

2 In the preceding section, we derived the diffraction field $\mathbf{M}_1^{\theta}(x, y; \mathrm{dr})$ generated
3 by a differential edge at an arbitrary orientation. By performing the path integration of
4 this field along all the mask edges, we constructed a full-chip covariant edge
5 diffraction response $\mathbf{M}_1$:

6
$$\mathbf{M}_1[\partial A(x, y)] = \oint_{\mathrm{edge}} \mathbf{M}_1^{\theta}(x, y; \mathrm{r})\mathrm{dr} \quad (10)$$

7 To efficiently construct the edge correction term $\mathbf{M}_1[\partial A(x, y)]$ for full-chip
8 curvilinear masks, we propose an algorithm that realises the path integral via
9 nine-channel convolution, with reference to Eqs. (8) and (9). The detailed
10 implementation workflow is shown in Fig. 4.

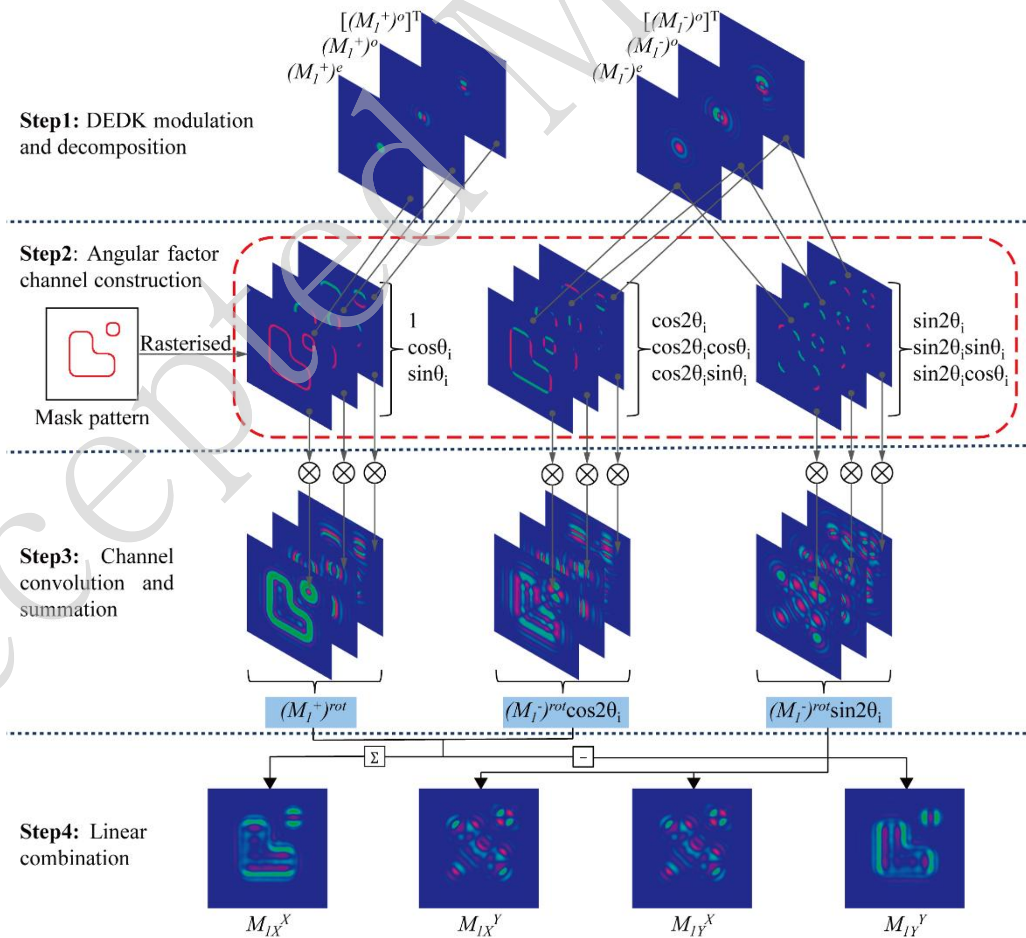

11

Accepted Manuscript

ACCEPTED ARTICLE PREVIEW

1 **Fig. 4** Workflow of the nine-channel convolution algorithm for curvilinear mask path integration.
2 Step 1: The DEDK undergoes a rotational similarity transformation and an adjoint rotation, and is
3 decomposed into the basis set $\left\{\{(M_1^+)^e,(M_1^+)^o,[(M_1^+)^o]^T\};\{(M_1^-)^e,(M_1^-)^o,[(M_1^-)^o]^T\}\right\}$. Step 2:
4 The full-chip mask pattern is discretised. For each edge segment with a normal angle θ_i, the
5 angular factors are computed and rasterised into nine image channels, formed by the tensor
6 product $\{1, \cos 2\theta_i, \sin 2\theta_i\}\otimes\{1, \cos\theta_i, \sin\theta_i\}$. Step 3: The kernel set is convolved with the
7 corresponding angular factor images, and the results are summed to obtain the full-chip
8 Jones-matrix distribution components $(M_1^+)^{rot}, (M_1^-)^{rot}cos2\theta_i$ and $(M_1^-)^{rot}sin2\theta_i$. Step 4:
9 These components are linearly combined according to Eq. (9) to synthesise the edge correction
10 term $\mathbf{M_1}$.

11 First, the DEDK Jones matrix was transformed by rotational similarity, yielding the
12 modulated kernels M_1^+ and M_1^-. Simultaneously, the adjoint rotation of the
13 modulated kernels was expressed as a linear combination of circular harmonic basis
14 functions. Accordingly, the modulated kernels were decomposed into the following
15 basis sets: $\{\{(M_1^+)^e,(M_1^+)^o,[(M_1^+)^o]^T\};\{(M_1^-)^e,(M_1^-)^o,[(M_1^-)^o]^T\}\}$. Subsequently, the
16 full-chip mask edges were discretised. For each sufficiently short edge segment with a
17 normal angle θ_i, the corresponding angular factors were rasterised into image channels.
18 The angular factor channels consisted of the tensor-product combination of two sets
19 of rotation representations: the Jones-matrix rotational similarity terms $\{1, \cos 2\theta_i,$
20 $\sin 2\theta_i\}$ and the adjoint rotation terms of the kernel $\{1, \cos\theta_i, \sin\theta_i\}$, resulting in nine
21 channels. The kernel set was then convolved with the corresponding angular factor
22 images and summed to obtain the full-chip Jones-matrix distribution components
23 $(M_1^-)^{rot}cos2\theta_i$, $(M_1^-)^{rot}sin2\theta_i$ and $(M_1^+)^{rot}$. Finally, these components were
24 linearly combined to synthesise a full-chip edge diffraction correction term. This
25 method accommodated the curvilinear edges of an arbitrary orientation, thereby
26 overcoming the limitations of traditional Manhattanisation models that support only a
27 few fixed directions, whereas the rotational similarity transformation of the Jones

Accepted Manuscript

matrix guaranteed physical covariance. Moreover, by employing image convolution, the full-layout mask diffraction response could be rapidly constructed without explicit kernel rotation, thereby significantly improving modelling efficiency.

In the final synthesis stage, the edge diffraction term $\mathbf{M_1}[\partial A(x, y)]$ was superimposed with the thin-mask component $\mathbf{M_0}[A(x, y)]$ to yield the complete curvilinear thick-mask model $\mathbf{M}(x, y)$, as illustrated in Fig. 5.

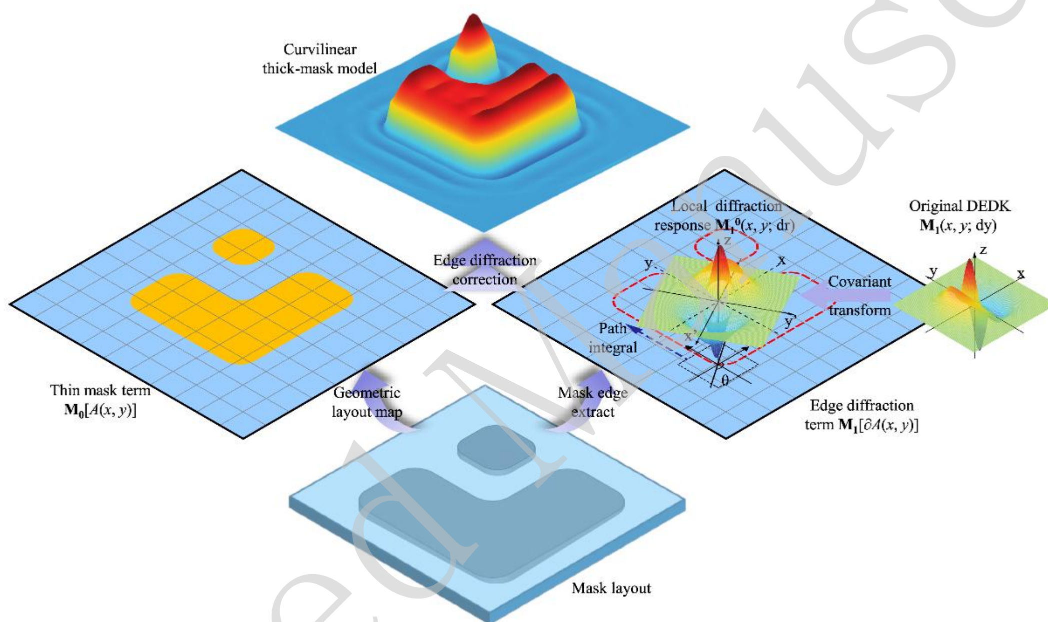

Fig. 5 Workflow for constructing a physically covariant curvilinear thick-mask model with edge diffraction correction. Starting from the mask layout, the thin-mask term $\mathbf{M_0}[A(x, y)]$ is generated by mapping the geometric layout distribution. Geometric edges are then extracted, and the precomputed DEDK $\mathbf{M_1}(x, y; \mathrm{dy})$ is loaded. For each differential edge segment dr with a normal angle θ relative to the x-axis, its diffraction response is computed using the covariance transform in Eq. (9). By integrating these local responses along the entire edge path, the physically covariant edge diffraction correction $\mathbf{M_1}[\partial A(x, y)]$ is assembled. Finally, the thin-mask term $\mathbf{M_0}[A(x, y)]$ and the edge diffraction term $\mathbf{M_1}[\partial A(x, y)]$ are linearly superposed to form the curvilinear thick-mask model **M**.

This hierarchical approach ensured computational scalability while preserving the

Accepted Manuscript

ACCEPTED ARTICLE PREVIEW

physical covariance for arbitrary edge orientations. By implementing nine-channel image convolutions to perform DEDK path integration along the mask edges, this method enabled efficient full-chip mask simulation. Consequently, it provided a physically covariant, rapid, and full-chip modelling solution for curvilinear masks, enabling accurate and efficient forward modelling for CL.

Results

Accuracy and efficiency of mask near-field

We quantified the accuracy of the proposed curvilinear thick-mask model by comparing the near-field amplitude distributions with the benchmark solutions obtained through rigorous FDTD simulations. To demonstrate the universality of the model, we applied it to both Manhattan structures and arbitrary curvilinear layouts and compared the deviation of each case against the FDTD reference.

The initial validation focused on the accuracy of the proposed model in simulating the Manhattan mask layouts. Fig. 6a shows the localised metal layer layout for the Manhattan geometries with a CD of 45 nm. Unless otherwise specified, all the mask dimensions mentioned in this study refer to the wafer scale. Using the $\mathbf{E}_{\mathbf{X}}^{\mathbf{X}}$ component generated under X-polarised illumination as an example, Fig. 6b shows the near-field simulation results for the Manhattan layout using the rigorous FDTD simulation, Kirchhoff thin-mask approximation, and proposed thick-mask models. Based on the simulation results, the Kirchhoff approximation yielded a root mean square (RMS) error of 0.1007 and a maximum absolute (MA) error of 0.8088, whereas the proposed model achieved an RMS error of 0.0336 and an MA error of 0.2901. These results demonstrate that the proposed model significantly enhances the accuracy of the thin-mask approximation, reducing both the RMS and MA errors by approximately 3×, thereby confirming its efficacy in simulating thick masks in Manhattan mask layouts.

Accepted Manuscript

1 Curvilinear masks represent the key application scenarios targeted by the proposed
2 model. Simulation experiments validated the accuracy of the model in the near-field
3 modelling of curvilinear mask layouts. Fig. 6c shows a typical curvilinear mask layout
4 with a CD of 45 nm and its local magnified view. The mask layout comprised slanted
5 edge segments and rounded corner curve segments, and was characterised by a
6 discretised set of sampling points collected along the mask edges. Fig. 6d compares
7 the near-field distributions across the four polarisation components of the curvilinear
8 mask generated using the rigorous FDTD, thin-mask, Manhattanisation thick-mask,
9 and proposed models.

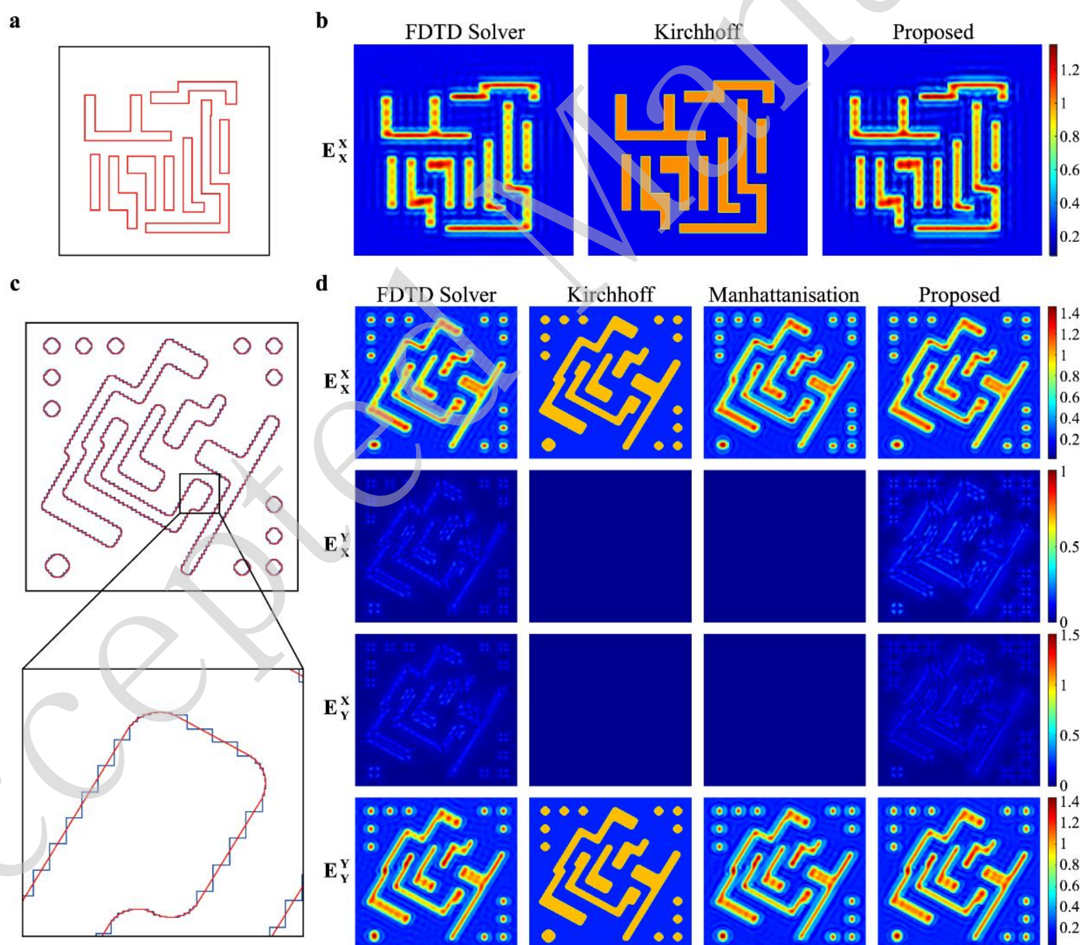

10

11 **Fig. 6** Comparison of near-field modelling results for mask layouts via different modelling
12 methods. **a** Manhattan mask layout with a CD of 45 nm. **b** Near-field distributions of the mask

Accepted Manuscript

ACCEPTED ARTICLE PREVIEW

1 layout generated using the FDTD, thin-mask, and proposed models. **c** Curvilinear mask layout
2 with a CD of 45 nm and its local magnification. The red line represents the original curvilinear
3 mask geometry, composed of slanted segments and circular arc segments, characterised through
4 discretised edge-sampling point sets. The blue line denotes the Manhattanisation layout,
5 represented by orthogonal horizontal–vertical segments. **d** Near-field distributions of the
6 curvilinear mask generated using the FDTD, thin-mask, Manhattanisation thick-mask, and
7 proposed models.

8 The Manhattanisation thick-mask model approximates a curvilinear mask by
9 breaking it into horizontal and vertical segments. The corresponding kernels were
10 selected from a precomputed kernel library at the orientations of 0°, 90°, 180°, and
11 270°, convolved with the edge segments, and then linearly combined with the
12 thin-mask term to produce the near-field distribution. To ensure a fair comparison,
13 this model used the same rigorous simulation data source, thin-mask baseline, and
14 kernel extraction method as the proposed model. The maximum edge displacement
15 (MED), defined as the Hausdorff distance between the Manhattanised polygons and
16 original curves, serves as a critical metric for evaluating the geometric fidelity after
17 Manhattanisation and directly controls the accuracy of this approach [40]. The
18 convergence curve of the near-field deviations in the Manhattanisation thick-mask
19 model was simulated as the MED was varied, and the results are shown in Fig. S1 in
20 the Supplementary Information. Based on the convergence curve, the MED for the
21 Manhattanisation model was set to 4 nm.

22 Table 2 summarises the RMS and MA errors along with the run times for each
23 method, using the rigorous FDTD results as the benchmark. The proposed model
24 achieved a two times smaller RMS error compared with the Manhattanisation model
25 while attaining a smaller MA error and faster run speed. Despite a run time
26 approximately 5.5 times longer than that of the efficient Kirchhoff approximation
27 method, the proposed model was dramatically faster than the rigorous FDTD

Accepted Manuscript

approach, reducing the computation time by a factor of approximately 2640. These results demonstrate the superiority of the proposed model for curvilinear masks, as it delivers higher numerical accuracy and computational efficiency than the existing thick-mask methods.

Table 2 Accuracy and efficiency metrics for mask modelling methods relative to FDTD

Model	RMS error	MA error	Run time (s)
FDTD			~6895
Kirchhoff	0.1204	0.8288	0.4
Manhattanisation (MED = 4 nm)	0.0601	0.3445	2.73
Proposed	0.02858	0.2841	2.61

We compared deviations between the near-field distributions generated by the proposed model and benchmark FDTD simulations across various CDs and curvilinear mask layouts to validate the applicability of the proposed model, and the results are presented in Fig. S2 in Supplementary Information.

Imaging accuracy

We imported the curvilinear mask near-field described in Fig. 6d into a Hopkins imaging system to quantitatively evaluate the impact of the mask model accuracy on the aerial image fidelity within the CL workflow [41]. Fig. 7a shows an X-polarised quadrupole illumination pupil, whereas Fig. 7b compares aerial images and deviations across different mask models, with the aerial image derived from the near field generated using FDTD as the benchmark. Table 3 presents the quantitative analysis results.

Accepted Manuscript

ACCEPTED ARTICLE PREVIEW

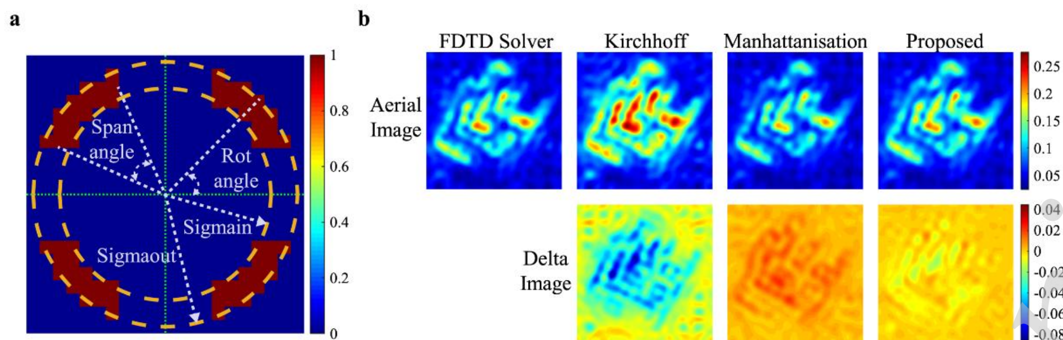

1

2 **Fig. 7** Aerial image simulation and accuracy verification of curvilinear mask based on Hopkins
3 imaging method. **a** Quadrupole illumination pupil with span angle = 45°, rot angle = 45°, sigmain
4 = 0.8, sigmaout = 1.0. **b** Aerial images and comparison results generated using the Hopkins
5 method under different mask models

6 **Table 3** Error metrics of aerial images relative to FDTD

Model	RMS error	MA error
Kirchhoff	0.02719	0.08666
Manhattanisation	0.006818	0.02233
Proposed	0.003297	0.01903

7 Compared with the imaging results derived from the Kirchhoff and
8 Manhattanisation mask models, the proposed method decreased the RMS error by
9 87.9% and 51.6%, respectively, and decreased the MA error by 78.0% and 14.8%,
10 respectively. This comparative analysis demonstrates that the proposed curvilinear
11 thick-mask model delivers superior imaging accuracy compared with existing models
12 in a CL system.

13 **Validation of physical covariance of mask models**

14 Full-chip mask layouts frequently contain numerous repetitive units. Mask models
15 must provide physically consistent representations of these units. This requirement is
16 fundamental to semiconductor manufacturing and is governed by the principle of the
17 physical covariance of electromagnetic effects. A key metric for assessing this
18 property is the invariance of the model under coordinate transformations, which

Accepted Manuscript

ACCEPTED ARTICLE PREVIEW

1 encompasses both translational and rotational invariances. Fig. 8a shows the
2 workflow used to validate the physical covariance of the mask models. First, the
3 near-field distribution $\mathbf{N_1}$ of the original mask layout was generated using the mask
4 model as a reference. The mask layout was then subjected to an arbitrary coordinate
5 transformation, such as translation or rotation, and re-simulated to obtain the
6 near-field $\mathbf{N_2}$. The inverse transformation was applied to $\mathbf{N_2}$ to restore it to the original
7 coordinates, yielding $\mathbf{N_2'}$. The deviation between $\mathbf{N_1}$ and $\mathbf{N_2'}$ quantitatively assesses
8 the invariance of the model. Fig. 8b shows the test mask layout used in the experiment,
9 which consisted of an array of rounded corner squares with a CD of 45 nm. The
10 near-field distributions generated by translating or rotating the test mask are presented
11 in the Supplementary Information (Fig. S3).

12 Fig. 8c plots the RMS and MA errors of each model under translational
13 invariance testing as a function of the mask translation distance. The curves reveal
14 that the proposed model reduced both RMS and MA errors by approximately 70%
15 relative to the Kirchhoff approximation while achieving accuracy comparable to that
16 of rigorous FDTD simulations. These results validate the translational invariance of
17 the proposed model, demonstrating that mask layout displacement has a negligible
18 impact on its near-field predictions.

Accepted Manuscript

ACCEPTED ARTICLE PREVIEW

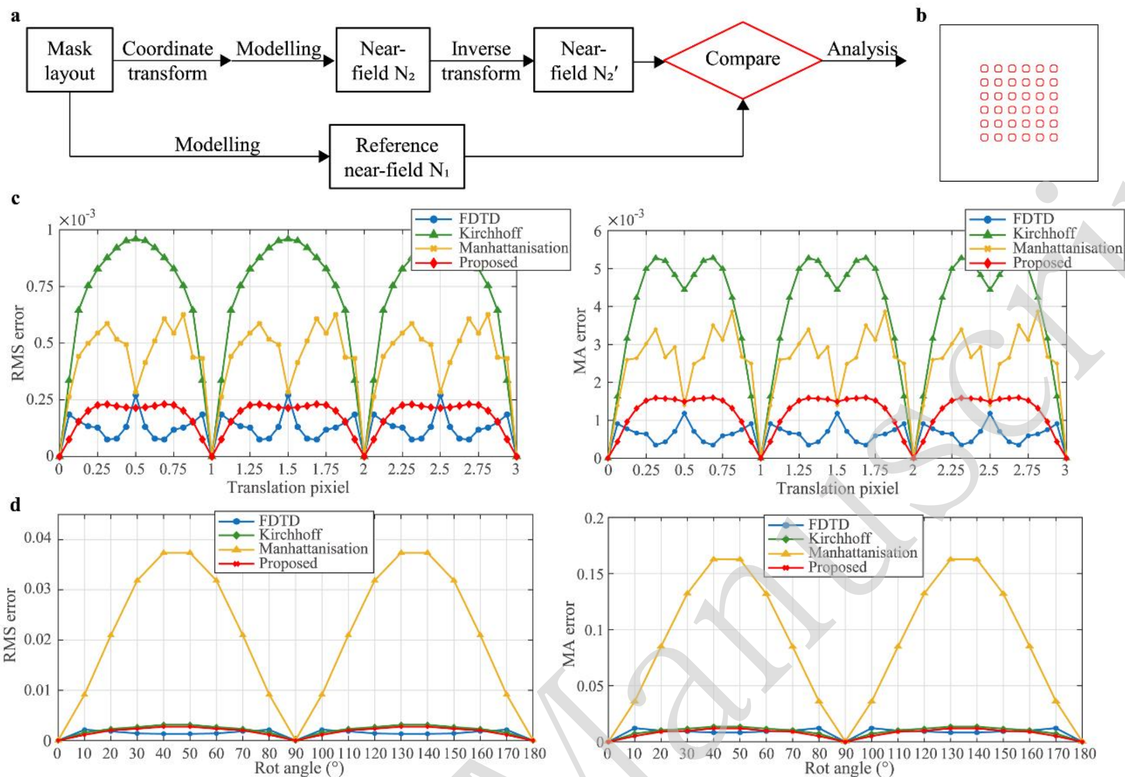

1

2 **Fig. 8** Experiment for verifying the physical covariance of the mask models. **a** Workflow for the
3 verification of the physical covariance of the mask models. **b** The test mask features an x–y
4 symmetric layout and consists of an array of rounded-corner squares with a CD of 45 nm and a
5 pitch of 90 nm. **c** RMS and MA errors vs. mask translation distance in the translational invariance
6 test. **d** RMS and MA errors vs. mask rotation angle in the rotational invariance test

7 Fig. 8d shows the RMS and MA error as functions of the mask rotation angle in
8 the rotational invariance test. An analysis of these curves indicates that the proposed
9 model reduced both the RMS and MA errors by approximately 90% compared with
10 the Manhattanisation thick-mask model, achieving rotational errors comparable to
11 those of the rigorous physical model. These results validated the rotational invariance
12 of the proposed model. Furthermore, the rotational errors approached zero at the
13 orientations of 90° and 180°, revealing the exceptional symmetry-preservation
14 capability of the proposed model.

Accepted Manuscript

ACCEPTED ARTICLE PREVIEW

Discussion

The aforementioned experiments validated the performance of the proposed model in terms of accuracy, efficiency, and universality. For DUV lithography at the 45 nm node and below, the proposed model enabled the efficient construction of thick-mask near-field distributions that accurately reflect 3D mask topography. Compared with the existing Manhattanisation thick-mask model, the proposed model exhibited superior computational accuracy and efficiency when handling curvilinear mask layouts. This advantage originates from the fact that Manhattanisation requires a strict control of the MED across complex full-chip curvilinear mask layouts, which imposes additional computational overhead and introduces modelling errors. Furthermore, as explained in the principal section, the mask edge diffraction can be decomposed into even and odd field components, where the even component is scalar and dependent exclusively on the total edge length. As Manhattanisation alters the edge length (see Fig. 6c), it inevitably introduces an additional error term that degrades near-field modelling accuracy.

In terms of the validation of physical covariance, the rotational invariance test showed that the Manhattanisation model approximated curvilinear edges with horizontal–vertical segments, generating distinct geometric layouts at different rotation angles, thus breaking rotational invariance. By contrast, the proposed model extracted DEDKs and established a nine-channel tensor convolution architecture, achieving real-time covariant mapping between DEDKs and curvilinear edges at arbitrary orientations. This allowed the model to directly process curvilinear masks represented by discretised edge-sampling point sets, and it could be extended to other parametrically characterised geometries, termed 'MULTIGON' [18]. By fundamentally avoiding Manhattanisation geometric approximations, the proposed model delivered higher predictive fidelity and achieved a physical covariance comparable to that of a rigorous physical model. Note that, in the translational invariance tests, the translation

Accepted Manuscript

ACCEPTED ARTICLE PREVIEW

error of the model exhibited evident pixel-level periodic fluctuations. This indicated that the subpixel errors introduced by spatial discretisation remained a source of inaccuracy in the current model, warranting further reduction in future studies.

In summary, this paper proposed a physically covariant curvilinear thick-mask model based on edge diffraction correction for a rapid full-chip layout simulation. First, we expanded the mask transmission function into a series and truncated it into a linear combination of the thin-mask approximation term and an edge diffraction correction term. Through rigorous electromagnetic simulations, we derived physically meaningful 2D DEDKs and performed path integration along all the mask edges to reconstruct the full-chip edge diffraction term. Finally, this correction term was incorporated into the thin-mask approximation, yielding a rapid, physically curvilinear, thick-mask model. By comparing the near-field distributions across diverse mask layouts and quantifying the deviations between the generated aerial images and the benchmark, the proposed model achieved a 3× smaller error than the thin-mask model. Furthermore, the thick-mask model improved the computational efficiency by 2640 times relative to the rigorous physical model, validating its efficiency and universality. In curvilinear layouts, our method avoided the geometric Manhattanisation errors of traditional thick-mask models, thereby significantly enhancing the accuracy while overcoming the degradation of physical covariance in mask electromagnetic effects. Furthermore, translational and rotational invariance tests confirmed that the proposed model achieved a 10× improvement in rotational invariance over the Manhattanisation model while maintaining a performance comparable to those of rigorous physical models, thereby validating its reliability. Thus, this model provides robust support for efficient and accurate forward modelling in CL resolution-enhancement techniques, such as ILT and source mask optimisation.

Materials and methods

Mask materials and structures

Accepted Manuscript

ACCEPTED ARTICLE PREVIEW

1 Simulation experiments were performed based on a standard phase-shift mask, and
2 the material properties and geometric configurations are listed in Table 4. The
3 thin-mask transmission coefficients t_{bright} and t_{dark} in Eq. (3) were calculated using the
4 thin-film transfer matrix method using these parameters [37]. The same configuration
5 was adopted for rigorous simulations.

6 **Table 4** Phase-shift mask material and structural parameters

Material	n	k	Thickness (nm)	Sidewall angle (°)
SiO_2	1.56	0		
MoSi	2.43	0.6	69	90

7 **Numerical simulation**

8 The experiments were conducted using a 193 nm immersion DUV lithography
9 system equipped with 4× reduction optics and an NA of 1.35. To evaluate the
10 accuracy of the model rigorously, the FDTD electromagnetic solver in ANSYS
11 Lumerical was employed as a benchmark. Convergence analysis was performed for
12 the FDTD benchmark to establish a gold standard reference. The simulations were set
13 up with a discrete grid size of 4 × 4 × 2 nm on the mask scale, employing periodic
14 boundary conditions in the xy-direction and perfectly matched layers along the
15 z-direction.

16 A convergence test of the reference mask near-field versus the simulation domain
17 size was performed to determine a sufficiently large simulation domain, as shown in
18 Fig. 1b, and to eliminate edge-coupling effects. The results are shown in Fig. S4 in the
19 Supplementary Information. To balance the computational cost and accuracy, a
20 domain size of 18 wavelengths was chosen for the FDTD simulation and the
21 extraction of DEDKs.

22 In the near-field simulation experiments shown in Figs. 6 and 8, the simulation
23 region was 1024 × 1024 nm, corresponding to the wafer scale. The near-field image
24 grid resolution for the thin-mask, Manhattanisation thick-mask, and proposed models

Accepted Manuscript

ACCEPTED ARTICLE PREVIEW

was 4 × 4 nm at the wafer scale. The image size was 256 × 256 × 4, corresponding to the $\mathbf{E}_{\mathbf{X}}^{\mathbf{X}}$, $\mathbf{E}_{\mathbf{X}}^{\mathbf{Y}}$, $\mathbf{E}_{\mathbf{Y}}^{\mathbf{X}}$, $\mathbf{E}_{\mathbf{Y}}^{\mathbf{Y}}$ components of the near field. For the FDTD simulations, rigorous simulations were performed under both X- and Y-polarisations to obtain the corresponding near-field components. Because of the reduction factor of the lithography system, the size of the FDTD near-field image was 1024 × 1024 × 4. The FDTD results were subsequently processed through frequency-domain resampling and served as a benchmark for evaluating the performance of the proposed model.

In the validation experiments of the physical covariance, the low-pass filtering characteristics of the lithographic system were considered [32]. All the near-field deviation results were filtered at the 2 × NA spatial-frequency cut-off to suppress high-frequency noise, enabling a focused comparison of the core CL model performance. In the translational invariance experiment, the curves in Fig. 8c were obtained by comparing the restored near-field distributions with those of the reference. Specifically, the test mask was translated to different positions along the x-direction under X-polarised illumination $\mathrm{E}_{\mathrm{X}}^{\mathrm{in}} = [1,0]^{\mathrm{T}}$, and the resulting near-field images were translated back to the initial position and compared with the reference. For rotational invariance validation, the mask near-field $\mathbf{N}_1$ manifested the physical covariant properties governed by Eq. (7). The curves in Fig. 8d were obtained by rotating the test mask to different angles α, generating near-field distributions under linearly polarised illumination $\mathrm{E}_{\mathrm{in}} = [\cos\alpha, \sin\alpha]^{\mathrm{T}}$, applying the inverse rotation to map the results back to the original coordinate system, and then comparing them with the reference near-field image.

All simulation codes were implemented in C++ and executed on a personal computer with Intel Core i7-10700 CPU, 2.90 GHz, 64.0 GB of RAM.

Acknowledgements

This study was supported by the National Natural Science Foundation of China

Accepted Manuscript

ACCEPTED ARTICLE PREVIEW

(52130504 and 52205592), Major Program (JD) of Hubei Province (2025BEA006-4), Technology Innovation Program Project of Hubei Province (2024BAB013), and Major Program (JD) of Hubei Province (2023BAA008-2). The authors express their gratitude for the technical support provided by the Experiment Centre for Advanced Manufacturing and Technology at the School of Mechanical Science and Engineering at HUST. David H. Wei acknowledges productive discussions and collaborations with colleagues at Lanzhou University, where he provided a short course on lithography in July 2025.

Author contributions

Haofeng Chen: Writing—original draft, Validation, Software, Methodology, Investigation, Formal analysis, Data curation. Shaopeng Guo: Writing—original draft, Validation, Investigation, Formal analysis, Data curation. Kaixuan Su: Writing—original draft, Validation, Investigation, Formal analysis, Data curation. Song Zhang: Writing—review & editing, Validation, Software, Investigation, Funding acquisition, Formal analysis. Hao Jiang: Writing—review & editing, Supervision, Resources, Project administration, Methodology, Investigation, Funding acquisition, Conceptualization. David H. Wei: Writing—review & editing, Validation, Supervision, Software, Project administration, Methodology, Formal analysis, Conceptualization. Shiyuan Liu: Writing—review & editing, Supervision, Resources, Project administration, Investigation, Funding acquisition, Conceptualization.

Data availability

The data underlying the results and supplementary information presented in this paper are not publicly available at this time, but may be obtained from the authors upon reasonable request.

Accepted Manuscript

ACCEPTED ARTICLE PREVIEW

1 ## Conflict of interests

2 The authors declare the following: David H. Wei, Song Zhang and Shiyuan Liu have
3 financial interests in Yuwei Optica Co., Ltd., a company focusing on computational
4 lithography and holding patents related to technologies for lithography modelling
5 and applications.

6 ## References

7 1. Mack, C. A. Thirty years of lithography simulation. Proceedings of SPIE
8 5754, Optical Microlithography XVIII. San Jose: SPIE, 2005.

9 2. Erdmann, A. et al. Lithography simulation: modeling techniques and
10 selected applications. Proceedings of SPIE 7390, Modeling Aspects in
11 Optical Metrology II. Munich: SPIE, 2009, 13-29.

12 3. Ma, X. & Arce, G. R. Computational Lithography. (Hoboken: Wiley,
13 2010).

14 4. Lai, K. F. Review of computational lithography modeling: focusing on
15 extending optical lithography and design-technology co-optimization.
16 *Advanced Optical Technologies* **1**, 249-267 (2012).

17 5. Erdmann, A. et al. Optical and EUV projection lithography: a
18 computational view. *Microelectronic Engineering* **132**, 21-34 (2015).

19 6. Pomplun, J. et al. Reduced basis method for source mask optimization.
20 Proceedings of SPIE 7823, Photomask Technology 2010. Monterey:
21 SPIE, 2010, 78230E.

22 7. Pang, L. Y. et al. Study of mask and wafer co-design that utilizes a new
23 extreme SIMD approach to computing in memory manufacturing: full-chip
24 curvilinear ILT in a day. Proceedings of SPIE 11148, Photomask

Accepted Manuscript

ACCEPTED ARTICLE PREVIEW

1 Technology 2019. Monterey: SPIE, 2019, 111480U.

2 8. Granik, Y. Transformational invariance in compact process modeling.
3 *Journal of Micro/Nanolithography*, *MEMS*, *and MOEMS* **19**, 013502
4 (2020).

5 9. Liu, P. et al. Fast and accurate 3D mask model for full-chip OPC and
6 verification. Proceedings of SPIE 6520, Optical Microlithography XX. San
7 Jose: SPIE, 2007, 65200R.

8 10. Yan, Q. L., Deng, Z. J. & Shiely, J. Fast synthesis of topographic mask
9 effects based on rigorous solutions. Proceedings of SPIE 6730,
10 Photomask Technology 2007. Monterey: SPIE, 2007, 67302N.

11 11. Abrams, D. S. & Pang, L. Y. Fast inverse lithography technology.
12 Proceedings of SPIE 6154, Optical Microlithography XIX. San Jose: SPIE,
13 2006, 61541J.

14 12. Pang, L. Y. Inverse lithography technology: 30 years from concept to
15 practical, full-chip reality. *Journal of Micro/Nanopatterning*, *Materials*, *and*
16 *Metrology* **20**, 030901 (2021).

17 13. Shendre, A. & Fujimura, A. Leaping into the curvy world with
18 GPU-accelerated O(p) computing. *Journal of Micro/Nanopatterning*,
19 *Materials*, *and Metrology* **23**, 041505 (2024).

20 14. Kim, B. G. et al. Trade-off between inverse lithography mask complexity
21 and lithographic performance. Proceedings of SPIE 7379, Photomask
22 and Next-Generation Lithography Mask Technology XVI. Yokohama:
23 SPIE, 2009, 73791M.

24 15. Hooker, K. et al. Curvilinear mask solutions for full-chip EUV lithography.
25 Proceedings of SPIE 12054, Novel Patterning Technologies 2022. San

Accepted Manuscript

ACCEPTED ARTICLE PREVIEW

1 Jose: SPIE, 2022, 1205407.

2 16. Vidal-Russell, E. Curvilinear masks extend lithography options for
3 advanced node memory roadmaps. *Journal of Micro/Nanopatterning*,
4 *Materials, and Metrology* **23**, 041504 (2024).

5 17. Tomandl, M. et al. Multi-beam mask writing opens up new fields of
6 application, including curvilinear mask pattern for high numerical aperture
7 extreme ultraviolet lithography. *Journal of Micro/Nanopatterning*,
8 *Materials, and Metrology* **23**, 011205 (2024).

9 18. Choi, J. et al. Status of curvilinear data format working group.
10 Proceedings of SPIE 12325, Photomask Japan 2022: XXVIII Symposium
11 on Photomask and Next-Generation Lithography Mask Technology.
12 Online: SPIE, 2022, 1232508.

13 19. Pang, L. Y. & Fujimura, A. Why the mask world is moving to curvilinear.
14 *Journal of Micro/Nanopatterning, Materials, and Metrology* **23**, 041503
15 (2024).

16 20. Wei, D. H. et al. Mathematical foundations of a geometric theory of
17 diffraction for light scattering from a 3D topographic photomask.
18 Proceedings of 2019 Photonics & Electromagnetics Research
19 Symposium-Spring. Rome: IEEE, 2019.

20 21. Oskooi, A. F. et al. MEEP: a flexible free-software package for
21 electromagnetic simulations by the FDTD method. *Computer Physics*
22 *Communications* **181**, 687-702 (2010).

23 22. Ding, H. W. et al. Three-dimensional plasmonic lithography imaging
24 modeling based on the RCWA algorithm for computational lithography.
25 *Optics Express* **31**, 36061-36077 (2023).

Accepted Manuscript

1 23. Shao, F. et al. Fast rigorous simulation of mask diffraction using the
2 waveguide method with parallelized decomposition technique.
3 Proceedings of the 24th European Mask and Lithography Conference.
4 Dresden: VDE, 2008.

5 24. Adam, K. & Neureuther, A. R. Methodology for accurate and rapid
6 simulation of large arbitrary 2D layouts of advanced photomasks.
7 Proceedings of SPIE 4562, 21st Annual BACUS Symposium on
8 Photomask Technology. Monterey: SPIE, 2002.

9 25. Tirapu-Azpiroz, J., Burchard, P. & Yablonovitch, E. Boundary layer model
10 to account for thick mask effects in photolithography. Proceedings of
11 SPIE 5040, Optical Microlithography XVI. Santa Clara: SPIE, 2003.

12 26. Liu, P. et al. A full-chip 3D computational lithography framework.
13 Proceedings of SPIE 8326, Optical Microlithography XXV. San Jose:
14 SPIE, 2012, 83260A.

15 27. Zhu, K. Y. et al. Ultrasound modulated laser confocal feedback imaging
16 inside turbid media. *Optics Letters* **43**, 1207-1210 (2018).

17 28. Ma, X. et al. Fast lithography aerial image calculation method based on
18 machine learning. *Applied Optics* **56**, 6485-6495 (2017).

19 29. Ye, W. et al. TEMPO: fast mask topography effect modeling with deep
20 learning. Proceedings of 2020 International Symposium on Physical
21 Design. Taipei, China: ACM, 2020.

22 30. Li, Z. Q. et al. High-precision lithography thick-mask model based on a
23 decomposition machine learning method. *Optics Express* **30**,
24 17680-17697 (2022).

25 31. Shendre, A. et al. You don’t need 1nm contours for curvilinear shapes:

Accepted Manuscript

ACCEPTED ARTICLE PREVIEW

pixel-based computing is the answer. Proceedings of SPIE 12293, Photomask Technology 2022. Monterey: SPIE, 2022, 1229307.

32. Lam, M. et al. Accurate, full chip 3D electromagnetic field model for non-Manhattan mask corners. Proceedings of SPIE 9426, Optical Microlithography XXVIII. San Jose: SPIE, 2015, 94260P.

33. Zhang, H. B. et al. An accurate ILT-enabling full-chip mask 3D model for all-angle patterns. Proceedings of SPIE 8880, Photomask Technology 2013. Monterey: SPIE, 2013, 88800G.

34. Lai, C. J., Zhou, X. & Peng, D. P. Method of modeling a mask having patterns with arbitrary angles. (2021).

35. Natterer, F. The Mathematics of Computerized Tomography. (Philadelphia: SIAM, 2001).

36. Helgason, S. Geometric Analysis on Symmetric Spaces. 2nd edn. (Providence: American Mathematical Society, 2024).

37. Born, M. & Wolf, E. Principles of Optics: Electromagnetic Theory of Propagation, Interference and Diffraction of Light. 6th edn. (Oxford: Pergamon Press, 1980).

38. Zhou, X. J. et al. Efficient representation of mask transmittance functions for vectorial lithography simulations. *Journal of the Optical Society of America A* **31**, B10-B18 (2014)

39. Zhang, H. B. et al. A pattern- and optics-independent compact model of Mask3D under off-axis illumination with significant efficiency and accuracy improvements. Proceedings of SPIE 9426, Optical Microlithography XXVIII. San Jose: SPIE, 2015, 94260Q.

40. Chen, Y. Y. et al. Manhattan and curvilinear mask error correction.

Accepted Manuscript

ACCEPTED ARTICLE PREVIEW

Proceedings of SPIE 13216, Photomask Technology 2024. Monterey: SPIE, 2024, 132161M.

41. Guo, S. P. et al. Mask3D-compatible full-vectorial Hopkins imaging for lithographic modeling. *Optica* **12**, 924-934 (2025).

Accepted Manuscript